On Effective Material Parameters of Thin Perforated Shells under Static Loading

Stefano Giani[a], Harri Hakula[b]

[a] *Durham University*
School of Engineering and Computing Sciences
South Road, Durham, DH1 3LE, United Kingdom
[b] *Aalto University*
Department of Mathematics and System Analysis
P.O. Box 11100
FI–00076 Aalto, Finland

Abstract

One of the defining properties of thin shell problems is that the solution can be viewed as a linear combination of local features, each with its own characteristic thickness-dependent length scale. For perforated shells it is thus possible that for the given dimensionless thickness, the local features dominate, and problem of deriving effective material parameters becomes ill-posed. In the general case, one has to account for many different aspects of the problem that directly affect the effective material parameters. Through a computational study we derive a conjecture for the admissible thickness-ranges. The effective material parameters are derived with a minimization process over a set of feasible instances. The efficacy of the conjecture and the minimization process is demonstrated with an extensive set of numerical experiments.

Keywords:

1. Introduction

Engineering constructions made of perforated materials are challenging from the computational mechanics point-of-view. In recent years there has

Email addresses: stefano.giani@durham.ac.uk (Stefano Giani), Harri.Hakula@aalto.fi (Harri Hakula)

been much interest in new discretization methods designed to overcome problems in complicated domains. See for instance recent works on Trefftz-like FEM [1] and [2], and virtual elements [3]. One of the goals of simulations of such constructions in the engineering context is to *avoid* the complexities via homogenization of material parameters, the so-called *effective material parameters*.

The literature on perforated materials is somewhat sparse. The introduction in Martikka et al. [4] serves as an excellent overview of the complexities of perforated shell designs and their applications. In early works Forskitt [5] and Burgemeister [6] considered plates and established the terminology. Recently Jhung and his collaborators have published a number of papers within nuclear reactor design context, see [7], [8], [9]. For a detailed and exhaustive case study for a single cylindrical shell submerged in fluid, see [10].

In this paper it is assumed that the perforation patterns are parameterized but regular. Our focus is on thin perforated shells, a class of parameter-dependent problems, where the parameter is the dimensionless thickness. It is shown through carefully designed numerical examples that there exists a complex interplay between the perforation pattern, shell geometry, thickness, and the static loading.

One of the defining properties of thin shell problems is that the solution can be viewed as a linear combination of local features, each with its own characteristic parameter-dependent length scale. This is often referred to as *boundary layer resolution* with the understanding that some of the boundary layers can be internal [11]. In our context the homogenization process is interpreted as approximation of this linear combination with an equivalent one on a non-perforated domain. One of the main results of this work is that we demonstrate that given a fixed pair of perforation pattern and loading, there exists a *critical thickness* t_c at which the relative importance of the solution components changes and thus, a single homogenization process cannot be valid over all thicknesses. Since the boundary layer resolution depends on the shell geometry, this means that the value of the critical thickness depends on it as well. We adopt a convention where t is dimensionless, $t = d/L$, where d is the actual thickness and L is some characteristic length scale, for instance, the diameter of the domain. For our discussion we can use t and d interchangeably.

In Figure 1 the inherent complexity of homogenization in a parameter dependent case is illustrated. In all three subsplots the transverse deflection is shown over the cylinder. On the left (Figure 1a) the reference solution has

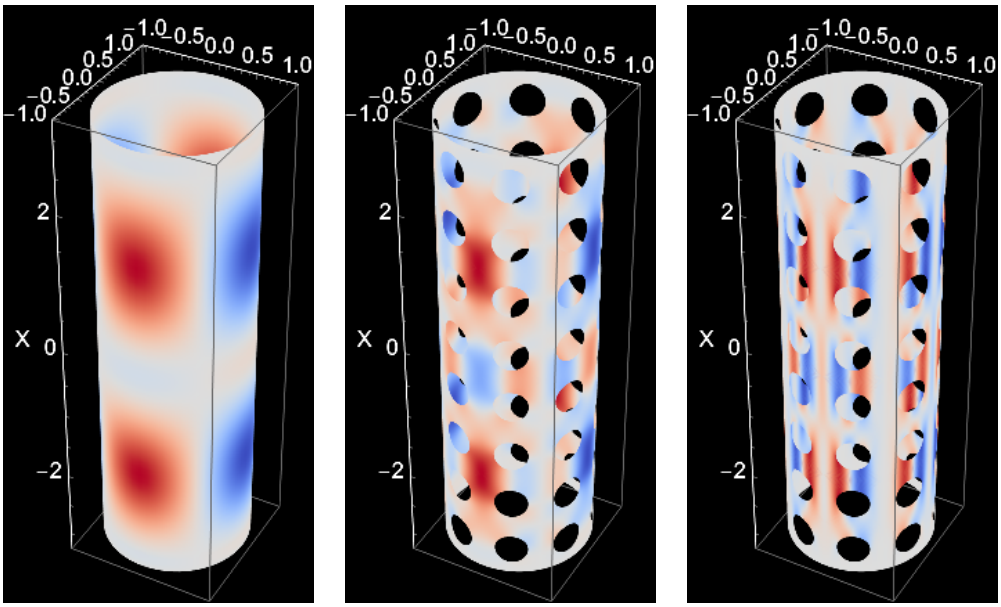

(a) Reference solution. (b) 8×8-grid; $t = 1/100$. (c) 8×8-grid; $t = 1/10000$.

Figure 1: Parabolic case: 3D visualization of transverse deflection; Loading $f(x, y) = \cos(2x)\cos(2y)$, $x \in [-\pi, \pi]$, $y \in [0, 2\pi]$ corresponding to radius $= 1$.

a distinct pattern which is also present in the perforated shell with $t = 1/100$ (Figure 1b). However, in the very thin case (Figure 1c) the *local* features dominate the solution and it is clear that a simple reparametrization of the material properties of the reference solution will not recover the features of the perforated one. In other words, in the linear combination of the local features with characteristic length scales, the dominant components can change as the parameter, dimensionless thickness, changes.

Of course it is very difficult to analyze these structures analytically. However, through computational studies we can state conjectures of the following type:

Conjecture. *For a perforated shell with $k\,\%$ of surface covered by circular holes laid in a $g \times g$-regular grid, the critical thickness t_c decreases as a function of cell size (grid density) $\epsilon = 1/g$ as*

$$t_c \sim C(k)\epsilon^2,$$

where $C(k)$ is a constant depending on k.

In practice the critical thickness t_c is not sharp. This will be discussed in detail in the context of numerical experiments. Assuming that the chosen thickness $t \geq t_c$, any multiplicative effective material parameter such as Young's modulus can be found through a minimization process in the chosen norm. Our choice is to minimize in L^2-norm over a representative domain, where the non-perforated solution is tested against an average of a sample of solutions with different grids or equivalently, values of ϵ. Interestingly, the derived effective material parameters do depend on the shell geometry. This means that deriving the parameters for a perforated plate does not necessarily lead to good results when curvature is introduced to the system. Every geometry should be handled separately.

The rest of this paper is structured as follows: In Section 2 necessary preliminaries are covered, including the shell models and geometry related features such as penetration patterns and a priori boundary layer resolution; Then in Section 3 the algorithm used in reference computations is outlined; The effective material parameters are discussed in Section 4; Our numerical experiments leading to conjectures are subject of Section 5 before conclusions of Section 6.

2. Preliminaries

In this section we establish the necessary background material for our numerical experiments. In particular we review the boundary layers associated with cylindrical shells and introduce the terminology used to describe the perforation patterns (*penetration patterns*).

2.1. Shell Model

Let us consider a dimensionally reduced linear shell model of Naghdi type for a shell consisting of homogeneous isotropic material with Poisson ratio ν. For theoretical justification for this model see [11]. The deformation of the shell is described in terms of a displacement field $\mathbf{u} = (u, v, w, \theta, \psi)$ defined on the shell midsurface ω. In addition to the tangential displacements u, v and the transverse displacement w, the vector field $\mathbf{u}$ consists of the dimensionless rotations θ, ψ related to the transverse shear deformations.

The total energy is given by a quadratic functional

$$\mathcal{F}(\mathbf{u}) = \frac{1}{2} D\mathcal{A}(\mathbf{u}, \mathbf{u}) - \mathcal{Q}(\mathbf{u}), \tag{1}$$

where $\mathcal{A}$ represents energy and $\mathcal{Q}$ is the load potential. The constant factor $D = E/(12(1-\nu^2))$, where E is the Young modulus of the material, and ν is the Poisson ratio.

Energy is further divided into bending, membrane, and shear energies, denoted by subscripts B, M, and S, respectively.

$$\mathcal{A}(\mathbf{u}, \mathbf{u}) = d^2 \mathcal{A}_B(\mathbf{u}, \mathbf{u}) + \mathcal{A}_M(\mathbf{u}, \mathbf{u}) + \mathcal{A}_S(\mathbf{u}, \mathbf{u}). \tag{2}$$

The energies are defined as

$$\begin{aligned}
\mathcal{A}_B(\mathbf{u}, \mathbf{u}) &= \int_\omega \left\{ \nu(\kappa_{11} + \kappa_{22})^2 + (1-\nu)(\kappa_{11}^2 + 2\kappa_{12}^2 + \kappa_{22}^2) \right\} \mathrm{d}\omega, \\
\mathcal{A}_M(\mathbf{u}, \mathbf{u}) &= 12 \int_\omega \left\{ \nu(\beta_{11} + \beta_{22})^2 + (1-\nu)(\beta_{11}^2 + 2\beta_{12}^2 + \beta_{22}^2) \right\} \mathrm{d}\omega, \\
\mathcal{A}_S(\mathbf{u}, \mathbf{u}) &= 6(1-\nu) \int_\omega \left\{ \rho_1^2 + \rho_2^2 \right\} \mathrm{d}\omega,
\end{aligned} \tag{3}$$

where β_{ij}, ρ_i, and κ_{ij} are the membrane, transverse shear, and bending strains, respectively.

2.1.1. Mathematical Shell Model

In the following we will simplify the model by assuming that ω is a domain expressed in the coordinates x and y. Furthermore, we assume that the curvature tensor $\{b_{ij}\}$ of the midsurface is constant and write $a = b_{11}, b = b_{22}$, and $c = b_{12} = b_{21}$. The shell is then called elliptic when $a\,b - c^2 > 0$, parabolic when $a\,b - c^2 = 0$, and hyperbolic when $a\,b - c^2 < 0$. The above assumptions are valid for example when the shell is shallow, i.e. the midsurface differs only slightly from a plane. In general the strain fields in (3) depend on the geometry of the shell. In the simplest case one may set $\mathrm{d}\omega = \mathrm{d}x\mathrm{d}y$ and write the relation between the strain and the displacement fields as

$$\begin{aligned}
\beta_{11} &= \frac{\partial u}{\partial x} + aw, \quad \beta_{22} = \frac{\partial v}{\partial y} + bw, \quad \beta_{12} = \frac{1}{2}\left(\frac{\partial u}{\partial y} + \frac{\partial v}{\partial x}\right) + cw, \\
\rho_1 &= \theta - \frac{\partial w}{\partial x}, \quad \rho_2 = \psi - \frac{\partial w}{\partial y}, \\
\kappa_{11} &= \frac{\partial \theta}{\partial x}, \quad \kappa_{22} = \frac{\partial \psi}{\partial y}, \quad \kappa_{12} = \frac{1}{2}\left(\frac{\partial \theta}{\partial y} + \frac{\partial \psi}{\partial x}\right).
\end{aligned} \tag{4}$$

This choice of shell model gives us additional flexibility in the design of the numerical experiments since the model admits *non-realizable* shell geometries.

2.1.2. Variational Formulation

By minimizing the the total energy (1) we can derive the variational problem: Find $\mathbf{u} \in \mathcal{U} \subset [H^1(\omega)]^5$ such that

$$\mathcal{A}(\mathbf{u}, \mathbf{v}) = \mathcal{Q}(\mathbf{v}) \quad \forall \mathbf{v} \in \mathcal{U}. \tag{5}$$

and the corresponding finite element problem: Find $\mathbf{u}_h \in \mathcal{U}_h$ such that

$$\mathcal{A}(\mathbf{u}_h, \mathbf{v}) = \mathcal{Q}(\mathbf{v}) \quad \forall \mathbf{v} \in \mathcal{U}_h. \tag{6}$$

The load potential has a form

$$\mathcal{Q}(\mathbf{v}) = \int_\omega \mathbf{f}(x, y) \cdot \mathbf{v}\; dx\, dy.$$

Let us consider a problem where the load acts in the transverse direction of the shell surface, i.e., $\mathbf{f}(x, y) = [0, 0, f_w(x, y), 0, 0]^T$. It can be shown that if for the load $\mathbf{f} \in [L^2(\omega)]^5$ holds, the problem (5) has a unique weak solution $\mathbf{u} \in [H^1(\omega)]^5$. The corresponding result holds in the finite dimensional case, when the finite element method is employed.

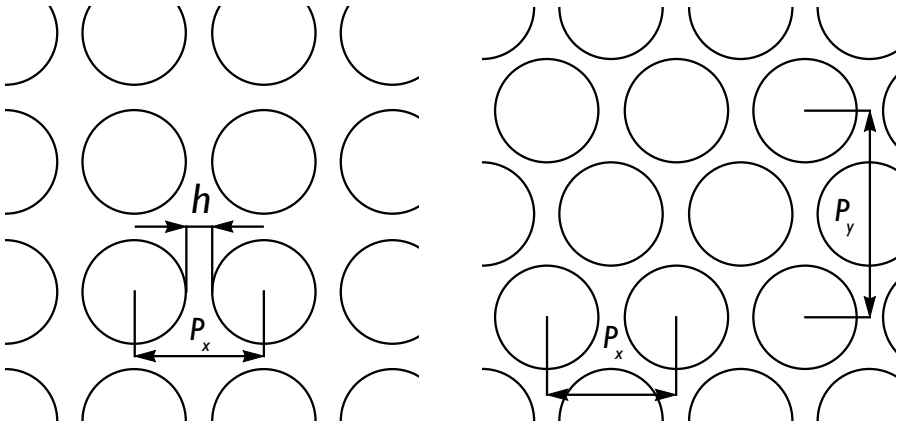

(a) Regular pattern (b) Triangular pattern

Figure 2: Penetration patterns

2.2. Penetration Patterns

The quantity used to characterize perforated sheets of metal is the ligament efficiency η. Let us assume that the holes are ellipses with a, b as the horizontal and perpendicular semiaxis, and the separation of the centres is P_x and P_y, respectively. Following [5], [6], [8], we define horizontal and perpendicular ligament efficiency, denoting them η_x, η_y, respectively. For regular arrays of holes

$$\eta_x = (P_x - 2\,a)/P_x, \qquad \eta_y = (P_y - 2\,b)/P_y, \tag{7}$$

and for triangular arrays, allowing for different layers,

$$\eta_x = (P_x - 4\,a)/P_x, \qquad \eta_y = (P_y - 4\,b)/P_y. \tag{8}$$

For circular holes the radius $r = a = b$, of course, and further if the pattern is regular $\eta = \eta_x = \eta_y$. Both pattern types are illustrated in Figure 2.

2.3. Layer Chart over Representative Cells

We follow the standard approach in homogenization and consider a representative domain or cell of size ϵ with one hole. Even though the shell problems are elliptic PDEs, the solutions may exhibit local features, formally boundary layers, with characteristic length scales much larger then the chosen ϵ. Therefore it is necessary to review the possible boundary layers that may occur in different scenarios.

For our discussion it is useful to define the concept of boundary layer generators first (see [11]).

Definition 1 (Layer Generator)**.** *The subset of the domain from which the boundary layer decays exponentially, is called the layer generator. Formally, the layer generator is of measure zero.*

The layer generators are independent of the length scale of the problem under consideration.

In perforated structures the hole boundaries are natural layer generators. The boundary layers are not concentrated only around the holes but can emanate along the characteristics of the shell surface. Elliptic, parabolic, and hyperbolic structures each posses a distinctive set of layer deformations. The layer structure is classically assumed to be an exponential solution to the homogeneous Euler equations of the shell problem. In Pitkäranta, Matache, and Schwab [11] it is shown using the Ansatz

$$\mathbf{u}(s, r) = \mathbf{U} e^{\lambda s} e^{ikr} \tag{9}$$

that solutions with $\mathrm{Re}\lambda < 0$ such that the characteristic lengths $L = 1/\mathrm{Re}\lambda \to 0$ are of the form $L \sim d^{1/n}$ where $n \in \{1, 2, 3, 4\}$. Here s is the coordinate orthogonal to the layer generator and r the one along it. From these the layer with $n = 2$ is present in all geometries whereas layers with $n = 3$ and $n = 4$ are present only in hyperbolic and parabolic geometries, respectively, and thus play a role here as well. The case $n = 1$, i.e., the shortest one arises from a shear deformation and can be captured by the shallow shell formulation, if necessary. In Figure 3 the layer chart is given both for the parabolic and hyperbolic representative cells, with the exception of the shortest one which is present on every boundary. For instance in the 3D visualizations for the very thin case (Figures 1c and 5c) the layer charts are clearly visible.

2.4. Numerical Locking

One of the numerical difficulties associated with thin structures is the so-called *numerical locking* which means unavoidable loss of optimal convergence rate due to parameter-dependent error amplification [12]. We use the p-version of the finite element method [13] in order to alleviate the (possible) locking and ensure convergence. Notice that even though the shell is strongly kinematically constrained or clamped, the perforations are free and thus bending can occur locally. In our experiments, the combination of choosing $p = 3$ and locally refined meshes is sufficient.

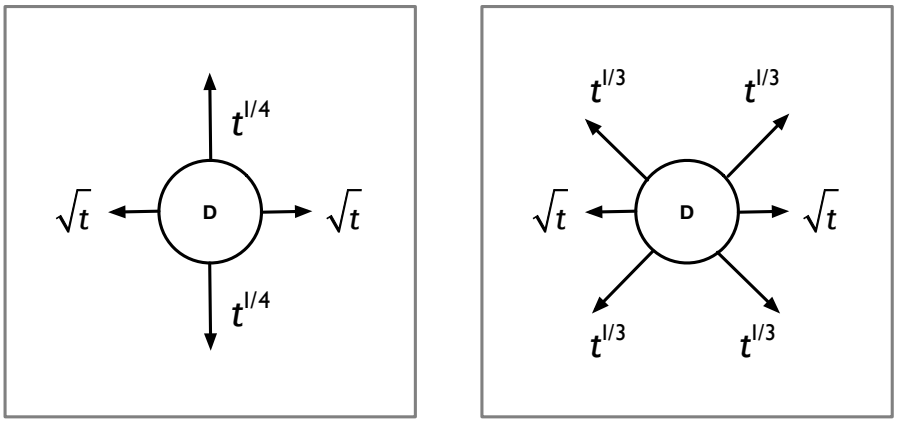

(a) Cylindrical shell. (b) Hyperbolic shell.

Figure 3: Representative cells: Layer charts with one hole D. The characteristic length scales are indicated in terms of the dimensionless thickness. In the hyperbolic case for the non-axial layers the direction depend on the actual geometry, in this case the decay is in the orthogonal direction to the one indicated by the arrow.

3. Solver

All the simulations are computed using a high-order continuous Galerkin code in 2D solving the variational formulation (6) on conforming meshes of triangular and quadrilateral elements. The code allows for any order of polynomials to be used in the elements, in fact, the presented results are computed using order $p = 3$ on meshes made of triangular elements.

In order to achieve good accuracy, the geometries of the holes are represented bending the elements around them using the transfinite interpolation method [14] which allow for the edges of the elements to be bent exactly to match the shape of the holes. In this way, any error arising from the geometrical representation of the domain on the mesh is avoided.

To reduce the computational time, the assembly of the linear system is done in parallel using MPI and the solution is computed in parallel using MUMPS [15, 16, 17] with MPI.

Due to the nature of this work that aims to present a new conjecture on how to apply homogenisation for shell problems and to highlight the limitations of the technique, it is mandatory that the accuracy of the computed solution is tested. In view of that, the code computes estimate the error η of the energy of the solution:

$$\eta := \sqrt{\mathcal{A}(\mathbf{u}_H - \mathbf{u}_h, \mathbf{u}_H - \mathbf{u}_h)}\ , \tag{10}$$

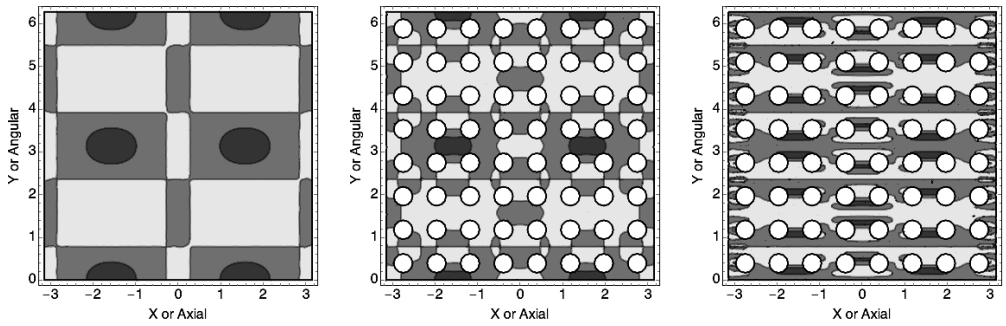

(a) Reference solution. (b) 8×8-grid; $t = 1/100$. (c) 8×8-grid; $t = 1/10000$.

Figure 4: Parabolic case: Contour plots of transverse deflection; Loading $f(x, y) = \cos(2x)\cos(2y)$, $x \in [-\pi, \pi]$, $y \in [0, 2\pi]$.

where $\mathbf{u}_H$ is the solution to be tested and $\mathbf{u}_h$ is the solution computed on a finer finite element space constructed completely and uniformly refining the mesh used for $\mathbf{u}_H$ and increasing the order p of polynomials by one in all elements. The same approach to estimating the error is used to drive the automatic mesh optimisation in [14]. Clearly, the computational cost to compute $\mathbf{u}_h$ is much greater than the cost to compute $\mathbf{u}_H$, but in the eyes of the authors, such cost is justified for the nature of the presented results.

4. Effective Material Parameters

In this section we first illustrate the interplay between the shell geometry, thickness, and loading for a fixed penetration pattern. Without any loss of generality in the definition of ϵ below we ignore the actual dimension 2π.

4.1. Asymptotics and Boundary Layers

Let us recall the Figure 1 above and consider the Figures 4–6. Simply by visual inspection it is clear that the varying thickness has a strong effect on the solution via local features and as can be seen both in Figure 1 and 4 do travel along the characteristics of the surface.

The chosen grid with $\epsilon = 1/8$ is chosen so that the first thickness $t = 1/100$ is sufficiently large for the homogenisation to be possible, yet $t = 1/10000$ is too small. In the next section we make this selection precise.

4.2. Critical Thickness

Let us consider both parabolic and hyperbolic cases with three loads and three hole coverages. Through computational experiments we arrive at the

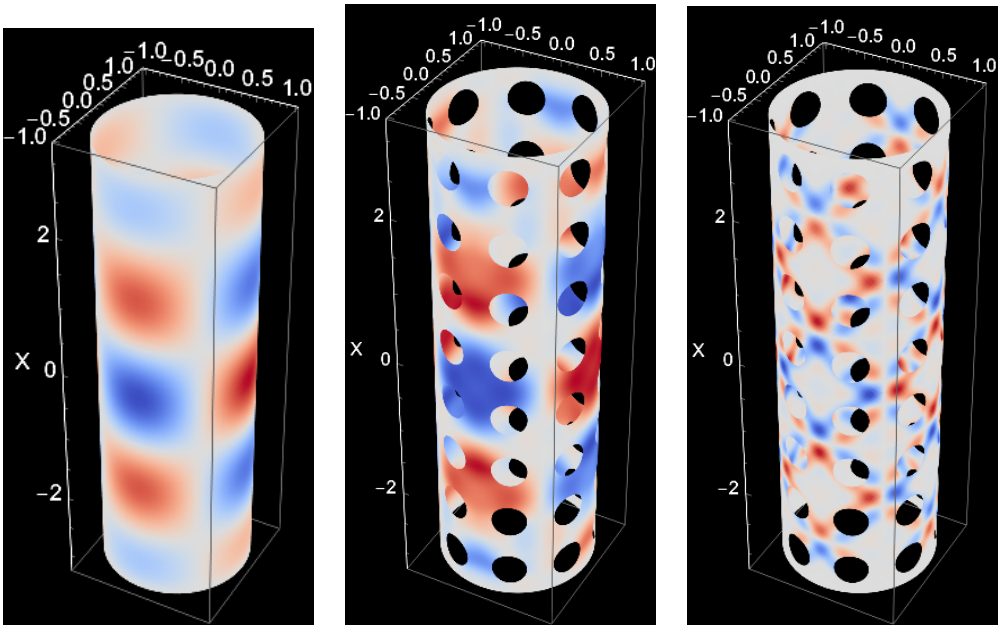

(a) Reference solution. (b) 8×8-grid; $t = 1/100$. (c) 8×8-grid; $t = 1/10000$.

Figure 5: Hyperbolic case: 3D visualization of transverse deflection; Loading $f(x, y) = \cos(2x)\cos(2y)$, $x \in [-\pi, \pi]$, $y \in [0, 2\pi]$ corresponding to radius $= 1$. Notice, that the actual surface is non-realizable.

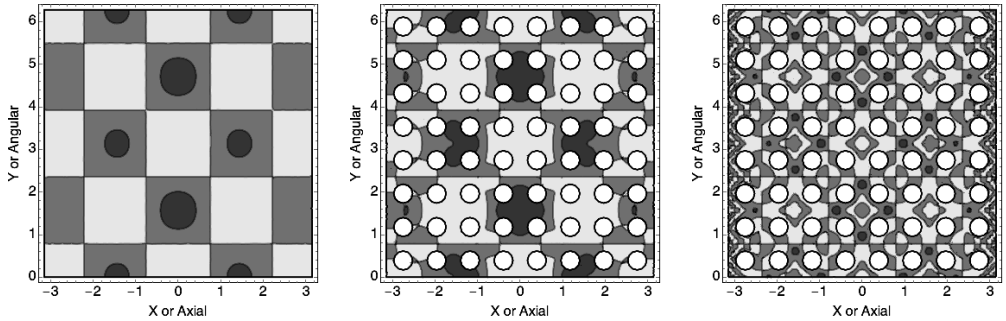

(a) Reference solution. (b) 8×8-grid; $t = 1/100$. (c) 8×8-grid; $t = 1/10000$.

Figure 6: Hyperbolic case: Contour plots of transverse deflection; Loading $f(x, y) = \cos(2x)\cos(2y)$, $x \in [-\pi, \pi]$, $y \in [0, 2\pi]$.

K	7%	12%	25%
0	(0.1,2.0)	(0.0,2.0)	(0.4,2.0)
1	(-0.9,2.1)	(-0.6,2.1)	(-0.8,2.2)
2	(0.9,2.2)	(1.1,2.1)	(1.4,2.2)

(a) Parabolic: (c, r); Most reliable at $K = 0$.

K	7%	12%	25%
0	(-0.1,2.0)	(-0.2,1.9)	(0.5,2.0)
1	(-1.3,2.1)	(-1.0,2.1)	(-0.6,2.2)
2	(-1.3,2.2)	(-1.2,2.2)	(-1.2,2.2)

(b) Hyperbolic: (c, r); Most reliable at $K = 0$.

Table 1: Observed rates of the critical thickness as a function of regular cell size (grid density) ϵ: $t_c \sim e^c \epsilon^r$, $\epsilon = 1/60, \ldots, 1$ (If the smallest t in the set is reached at $\epsilon > 1/60$, the smaller values of ϵ have been excluded); Loading is defined in terms of K: $f(x, y) = \cos(K\,x)\cos(K\,y)$, $x \in [-\pi, \pi]$, $y \in [0, 2\pi]$; Hole coverage is constant over all grids.

following conjecture relating the cell size ϵ and the *smallest thickness* with non-dominant local features, that is, the *critical* thickness t_c.

Conjecture 1. *For a perforated shell with k % of surface covered by circular holes laid in a $g \times g$-regular grid, the critical thickness t_c decreases as a function of cell size (grid density) $\epsilon = 1/g$ as*

$$t_c \sim C(k)\epsilon^2,$$

where $C(k)$ is a constant depending on k.

This conjecture can be related to the relative amount of bending energy in the system. In Table 2 and Figure 8 this connection is indicated in the case of constant loading but with multiple coverage percentages. As an ad hoc rule, the data suggests that when for any given configuration the bending energy is well below the 15% level, it is likely that the chosen dimensionless thickness is above the critical one.

4.3. Minimization over Representative Cell

Let us next focus on how to find the multiplicative effective material parameter once the critical thickness has been established. The goal is to find a solution u_0 to a non-perforated problem with a multiplicative constant α. Instead of operator formalism we use matrix notation and omit the dependence on the domain in matrices for now. Thus, in matrix notation the problem is

$$\alpha\, K u_0 = b,$$

where K and b are the stiffness matrix and the load vector, respectively. We proceed by choosing an admissible sequence of grids with ϵ_k, $k = 1, 2, \ldots, N$,

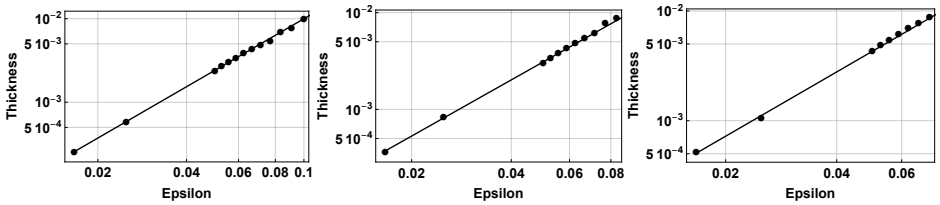

(a) Parabolic: 7%. (b) Parabolic: 12%. (c) Parabolic: 25%.

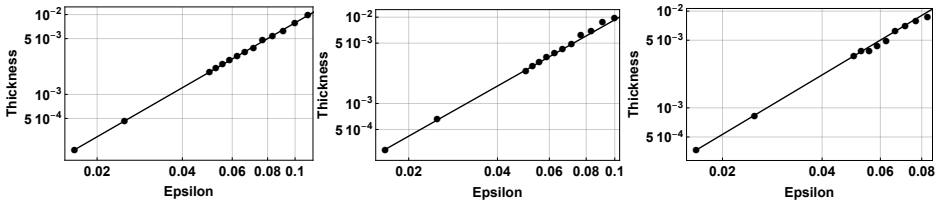

(d) Hyperbolic: 7%. (e) Hyperbolic: 12%. (f) Hyperbolic: 25%.

Figure 7: Convergence of the critical thickness t_c as a function of the cell size (grid density) ϵ at a given hole coverage; Loading is constant $f(x, y) = 1$; Only those grids where the expected solution profile is obtained are included; For both geometries the critical thickness is found at the highest value of ϵ, i.e., earliest, at 7%; Intercepts and rates are given in Table 1.

Geometry	Coverage	Prediction	15% Bending Level
Parabolic	7%	3×10^{-4}	2.6×10^{-4}
	12%	4×10^{-4}	3.7×10^{-4}
	25%	9×10^{-4}	5.0×10^{-4}
Hyperbolic	7%	2×10^{-4}	2.0×10^{-4}
	12%	3×10^{-4}	2.9×10^{-4}
	25%	4×10^{-4}	3.6×10^{-4}

Table 2: Comparison of critical thicknesses obtained through model prediction and 15% bending energy levels at a given hole coverage and fixed cell size (grid density) $\epsilon = 1/60$; Loading is constant $f(x, y) = 1$.

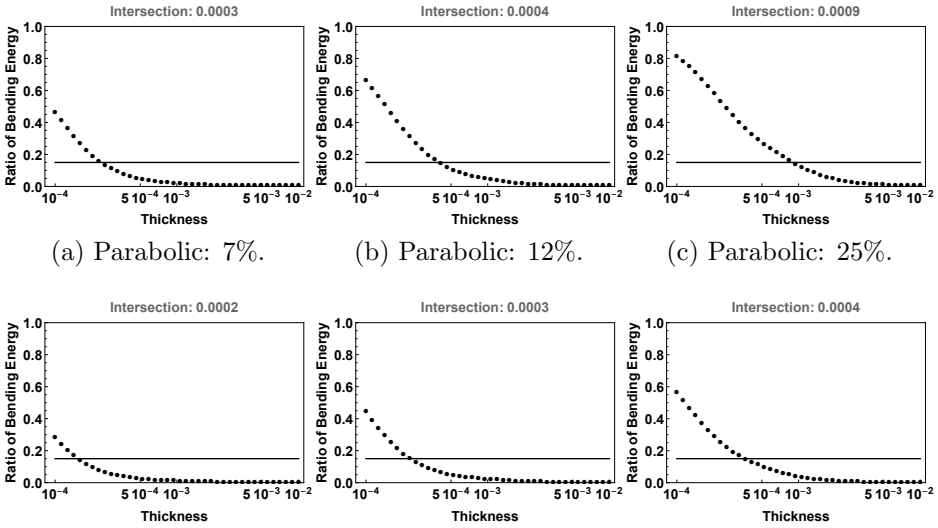

(a) Parabolic: 7%. (b) Parabolic: 12%. (c) Parabolic: 25%.

(d) Hyperbolic: 7%. (e) Hyperbolic: 12%. (f) Hyperbolic: 25%.

Figure 8: Percentage of the bending energy as a function of dimensionless thickness t at a given hole coverage and fixed cell size (grid density) $\epsilon = 1/60$; Loading is constant $f(x, y) = 1$; Reference level of 15% is indicated.

and finding the solutions to the perforated problems u_{ϵ_k}, $k = 1, 2, \ldots, N$. Formally, we seek u_0 as the minimizer for the sum of the squares of errors in the L^2-norm,

$$\min_{u_0 \text{ s.t. } \alpha K u_0 = b} \sum_k \|u_0 - u_{\epsilon_k}\|_{L^2}^2.$$

Denoting the standard mass matrix with M, finding α becomes a straighforward computation: First

$$\sum_k \|u_0 - u_{\epsilon_k}\|_{L^2}^2 = \sum_k (u_0 - u_{\epsilon_k})^T M (u_0 - u_{\epsilon_k}),$$

with $u_0 = (1/\alpha) K^{-1} b$, we get

$$= \sum_k ((1/\alpha) K^{-1} b - u_{\epsilon_k})^T M ((1/\alpha) K^{-1} b - u_{\epsilon_k})$$

$$= \sum_k ((1/\alpha)^2 (K^{-1} b)^T \, M \, K^{-1} b - \sum_k 2(1/\alpha)(K^{-1} b)^T \, M \, u_{\epsilon_k} + \text{const.}$$

Finally, we compute the minimum for $(1/\alpha)$ and take the reciprocal.

Putting everything together we have shown the following (formal) theorem

Theorem 2 (Formal)**.** *Let the thickness $t \geq t_c$ be given. Let us denote the stiffness and standard mass matrices as well as the load vector by K, M, and b, respectively. Let u_{ϵ_k}, $k = 1, 2, \ldots, N$, be a sequence of solutions of perforated problems with every ϵ_k sufficiently small. Then the homogenized solution u_0 is the minimizer of*

$$\min_{u_0 \ s.t. \ \alpha K u_0 = b} \sum_k \|u_0 - u_{\epsilon_k}\|^2_{L^2},$$

and α is the effective multiplicative constant

$$\alpha = N \frac{b^T K^{-1} M K^{-1} b}{\sum_k b^T K^{-1} M u_{\epsilon_k}}.$$

We have carefully labeled the theorem as formal since in practice the computational domain Ω depends on ϵ and thus the derived matrices as well as already noted above. Theoretically it is clear that for the mass matrices $\mathcal{M}_\epsilon \to M$ as $\epsilon \to 0$, but for the stiffness ones similar convergence cannot hold. Therefore, we constrain the minimization process to a subset shared by all computational domains, denoted by Ω_r,

$$\Omega_r \subset \Omega \text{ and } \Omega_r \subset \Omega(\epsilon_k), \quad k = 1, 2, \ldots, N.$$

In the context of this paper the simplest practical choice for Ω_r is to take it as the periodic line of symmetry or a collection of segments along it in the case of triangular penetration patterns. This choice has the added benefit of avoiding the boundary effects from the Dirichlet boundary conditions theoretically affecting the homogenization process.

Remark 3. *The scaling value α scales the non-perforated system matrix. Thus, lower values of α imply softer perforated structures since the loading is multiplied with a reciprocal. In particular, in standard setting one would expect the value of α decrease with the dimensionless thickness.*

5. Numerical Experiments

In the numerical experiments our aim is to demonstrate the effectiveness of the algorithms outlined above and show that the correct scalings depend

Category	Options
Geometry	Parabolic or hyperbolic
Penetration pattern	Regular or triangular
Loading	$f(x, y) = 1$ (constant) or $f(x, y) = \cos(x)\cos(y)$
Coverage	7% or 12 %
Thickness	$t = 1/100$ or $t = 1/1000$

Table 3: Overview of the experiments. Altogether 32 different configurations are covered by the experiments.

on the dimensionless thickness, the geometry of the shell, and the loading, forgetting neither the influence of the hole coverage nor the penetration pattern. The different categories of variables and their respective sets of values are given in Table 3.

5.1. Experimental Setup

The set of experiments consists of 32 cases. The penetration patterns and the related hole coverages correspond to practical, commercially available plates. The two thicknesses $t = 1/100$ and $t = 1/1000$ reflect the generally accepted bounds for realistic engineering structures. In all cases three grids have been used with $\epsilon_1 = 1/40$, $\epsilon_2 = 1/50$, $\epsilon_3 = 1/60$, respectively. For different statistics and qualitative assessment of the grids used, see Figure 9. We have opted not to vary the ligament efficiencies, but have constant values for 12% $\eta = 0.61$ and for 7% $\eta = 0.70$.

The qualitative reference solutions are illustrated as contour plots in Figures 10 and 11. One should notice that the local effects such as boundary layers in the case of constant loading can have a counterintuitive effect on the global solution if the discretization does not approximate all features of the solution. For instance, it would be natural to assume that the transverse deflection would increase as the dimensionless thickness decreases. In simulations, however, if the boundary layers are not properly resolved, then the maximal deflections are not either.

The quantitative energy error estimates are tabulated in Tables 4 and 5. In all setups two expected trends can be observed: As $t \to 0$ the total energy increases (without scaling of the load) and also the estimated error increases. This is due to the amount of bending energy at the free boundaries. The error estimate quantifies the improvement in the boundary layer resolution if

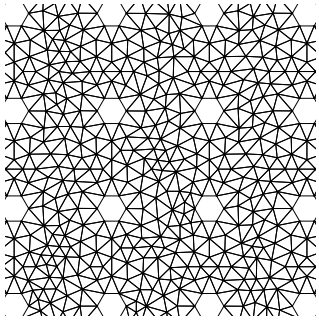

(a) Mesh detail: $\epsilon = 1/40$.

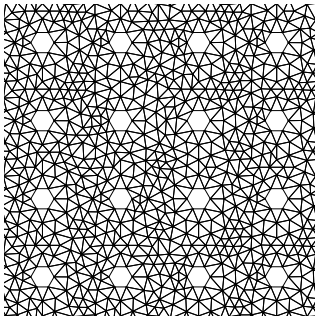

(b) Mesh detail: $\epsilon = 1/50$.

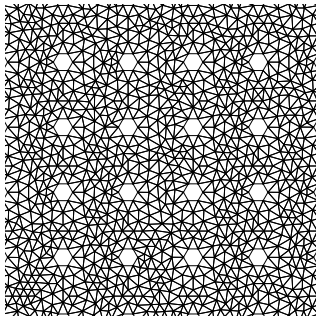

(c) Mesh detail: $\epsilon = 1/60$.

Pattern	Regular			Triangular		
ϵ	1/40	1/50	1/60	1/40	1/50	1/60
Nodes	6528	10208	14656	6808	10520	15028
Edges	17853	27913	40109	18596	28765	41134
Elements	9726	15206	21854	10128	15670	22416

(d) Statistics on the used meshes. Similar data for the error estimation varies case by case and is omitted.

Pattern	$\epsilon = 1/40$		$\epsilon = 1/50$		$\epsilon = 1/60$	
Regular	259698	(2626091)	404946	(3764591)	580946	(1743406)
Triangular	268786	(2698575)	416290	(3861336)	595866	(1751454)

(e) Statistics on the number of degrees of freedom for 7% coverage. The number in parentheses is the number of degrees of freedom used by the error estimator.

Figure 9: Statistical data on the meshes used in simulations. The mesh details are from the centre of the domain and cover the area $[-1/4, 1/4] \times [\pi - 1/4, \pi + 1/4]$. The holes are programmatically made geometrically correct with curved edges.

Thickness	ϵ	Regular		Triangular	
		Parabolic	Hyperbolic	Parabolic	Hyperbolic
1/100	1/40	3.53 (0.09)	2.39 (0.03)	3.64 (0.14)	2.48 (0.05)
	1/50	3.52 (0.08)	2.39 (0.03)	3.63 (0.14)	2.48 (0.05)
	1/60	3.52 (0.08)	2.39 (0.03)	3.63 (0.14)	2.48 (0.05)
1/1000	1/40	4.65 (0.62)	2.59 (0.14)	4.33 (0.60)	2.62 (0.09)
	1/50	4.13 (0.35)	2.51 (0.07)	3.98 (0.33)	2.58 (0.07)
	1/60	3.88 (0.22)	2.47 (0.05)	3.83 (0.23)	2.55 (0.06)

(a) Coverage 7%. Computed total energies with the error estimate in parentheses.

Thickness	ϵ	Regular		Triangular	
		Parabolic	Hyperbolic	Parabolic	Hyperbolic
1/100	1/40	3.43 (0.10)	2.15 (0.03)	3.88 (0.20)	2.37 (0.04)
	1/50	3.42 (0.09)	2.16 (0.02)	3.87 (0.20)	2.38 (0.04)
	1/60	3.42 (0.08)	2.16 (0.02)	3.87 (0.20)	2.37 (0.04)
1/1000	1/40	5.69 (1.95)	2.41 (0.15)	5.16 (1.44)	2.57 (0.11)
	1/50	4.53 (0.94)	2.29 (0.07)	4.46 (0.72)	2.50 (0.09)
	1/60	4.01 (0.53)	2.23 (0.05)	4.20 (0.46)	2.47 (0.08)

(b) Coverage 12%. Computed total energies with the error estimate in parentheses.

Table 4: Total energy and *hp*-error estimate: Constant load $f(x, y) = 1$.

Thickness	ϵ	Regular		Triangular	
		Parabolic	Hyperbolic	Parabolic	Hyperbolic
1/100	1/40	4.92 (0.47)	4.77 (0.41)	4.58 (0.32)	4.42 (0.28)
	1/50	4.92 (0.47)	4.79 (0.41)	4.57 (0.32)	4.44 (0.28)
	1/60	4.92 (0.46)	4.80 (0.40)	4.57 (0.32)	2.46 (0.28)
1/1000	1/40	5.30 (1.03)	5.27 (0.68)	5.31 (1.38)	5.02 (0.96)
	1/50	5.11 (0.70)	5.11 (0.56)	4.94 (0.85)	4.78 (0.60)
	1/60	5.03 (0.58)	5.01 (0.49)	4.78 (0.59)	4.66 (0.45)

(a) Coverage 7%. Computed total energies with the error estimate in parentheses.

Thickness	ϵ	Regular		Triangular	
		Parabolic	Hyperbolic	Parabolic	Hyperbolic
1/100	1/40	6.84 (0.82)	6.31 (0.69)	5.62 (0.48)	5.18 (0.40)
	1/50	6.84 (0.81)	6.34 (0.69)	5.59 (0.47)	5.22 (0.40)
	1/60	6.84 (0.81)	6.36 (0.69)	5.58 (0.47)	5.25 (0.40)
1/1000	1/40	7.67 (2.25)	7.53 (1.76)	7.85 (2.63)	6.73 (1.95)
	1/50	7.23 (1.41)	7.05 (1.27)	6.66 (1.41)	6.02 (1.08)
	1/60	7.05 (1.10)	6.77 (1.02)	6.16 (0.92)	5.70 (0.74)

(b) Coverage 12%. Computed total energies with the error estimate in parentheses.

Table 5: Total energy and *hp*-error estimate: Load $f(x, y) = \cos(x)\cos(y)$.

Thickness	Regular		Triangular	
	Parabolic	Hyperbolic	Parabolic	Hyperbolic
1/100	0.75	0.83	0.72	0.80
1/1000	0.66	0.71	0.72	0.78

(a) Coverage 7%.

Thickness	Regular		Triangular	
	Parabolic	Hyperbolic	Parabolic	Hyperbolic
1/100	0.65	0.78	0.57	0.70
1/1000	0.48	0.71	0.50	0.67

(b) Coverage 12%.

Table 6: Estimated values of the scaling factor α: Constant load $f(x, y) = 1$.

Thickness	Regular		Triangular	
	Parabolic	Hyperbolic	Parabolic	Hyperbolic
1/100	0.61	0.64	0.66	0.68
1/1000	0.59	0.60	0.61	0.63

(a) Coverage 7%.

Thickness	Regular		Triangular	
	Parabolic	Hyperbolic	Parabolic	Hyperbolic
1/100	0.36	0.41	0.45	0.49
1/1000	0.35	0.36	0.37	0.41

(b) Coverage 12%.

Table 7: Estimated values of the scaling factor α: Load $f(x, y) = \cos(x)\cos(y)$.

a refined *hp*-discretization were to be used. In the cases where the estimated error is relatively quite large the thickness is well-below the critical one.

5.2. Effective Material Parameters: Convergence

In this section we cover all 32 experiments and give a qualitative view of the effective scaling parameters α tabulated in Tables 6 and 7. All test cases are axially symmetric and thus along the midline $x = 0$ only the transverse deflection (w-component) is always nontrivial. In Figures 12 – 19 we show the profiles from three perforated cases, the reference, and the scaled reference result, that is, five profiles altogether. All in all, the agreement of the scaled profiles with the perforated ones is excellent. Notice, that the ranges are not scaled. In accordance with the theory of thin shell analysis, the relative oscillations increase as the dimensionless thickness tends to zero.

Let us consider the case of Figure 12. The perforation patterns are chosen using the graph of Figure 7. As noted already in the introduction, the critical thickness is not sharp. Even though the global wave number for the $t = 1/1000$ and $f(x, y) = 1$ is correct, the local oscillations are significant with ϵ_1. We emphasise that for these very thin shells, the strong feature at the symmetry line, i.e., $x = 0$ and $x = 2\pi$, is not physical but numerical artefact resulting from the ill-conditioned linear system of equations. Nevertheless, the minimisation process finds a more than reasonable value of α even in this case.

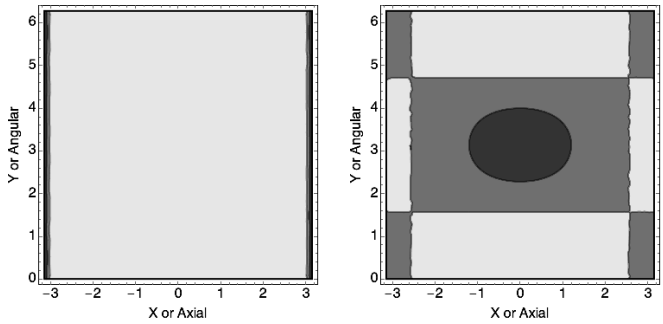

(a) $t = 1/100, K = 0$. (b) $t = 1/1000, K = 1$.

Figure 10: Parabolic reference solutions: Contour plots of the transverse deflection (w-component). Loading: $f(x, y) = \cos(Kx)\cos(Ky)$.

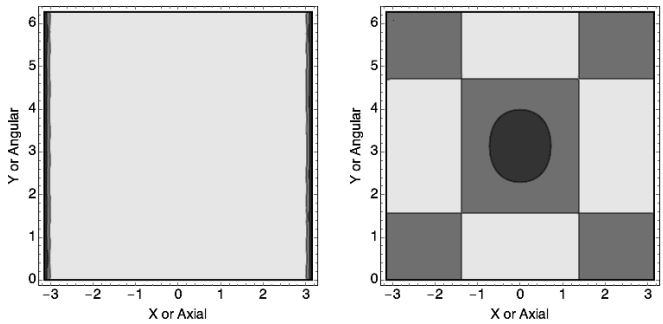

(a) $t = 1/100, K = 0$. (b) $t = 1/1000, K = 1$.

Figure 11: Hyperbolic reference solutions: Contour plots of the transverse deflection (w-component). Loading: $f(x, y) = \cos(Kx)\cos(Ky)$.

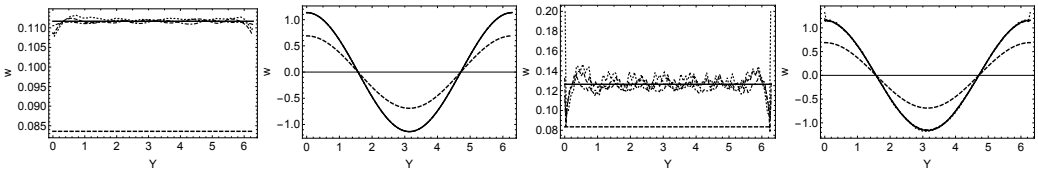

(a) $t = 1/100, K = 0$. (b) $t = 1/100, K = 1$. (c) $t = 1/1000, K = 0$. (d) $t = 1/1000, K = 1$.

Figure 12: Parabolic profiles at $x = 0$ (w-component). Regular penetration pattern. Hole coverage 7%. Three perforated solutions, the reference (dashed), and the effective reference (solid). Loading: $f(x, y) = \cos(Kx)\cos(Ky)$.

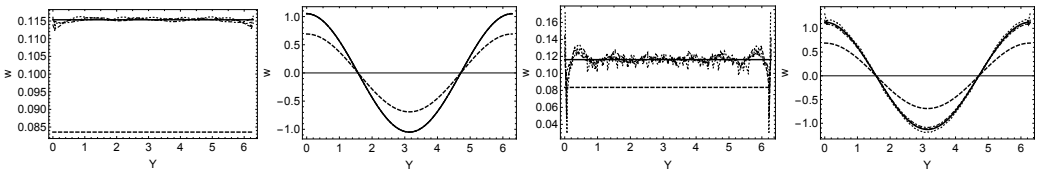

(a) $t = 1/100$,$K = 0$. (b) $t = 1/100$,$K = 1$. (c) $t = 1/1000$,$K = 0$ (d) $t = 1/1000$,$K = 1$.

Figure 13: Parabolic profiles at $x = 0$ (w-component). Triangular penetration pattern. Hole coverage 7%. Three perforated solutions, the reference (dashed), and the effective reference (solid). Loading: $f(x, y) = \cos(Kx)\cos(Ky)$.

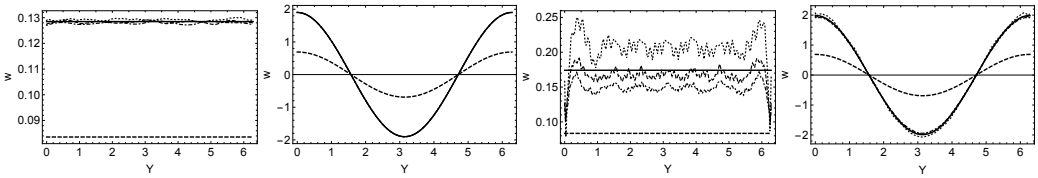

(a) $t = 1/100$,$K = 0$. (b) $t = 1/100$,$K = 1$. (c) $t = 1/1000$,$K = 0$ (d) $t = 1/1000$,$K = 1$.

Figure 14: Parabolic profiles at $x = 0$ (w-component). Regular penetration pattern. Hole coverage 12%. Three perforated solutions, the reference (dashed), and the effective reference (solid). Loading: $f(x, y) = \cos(Kx)\cos(Ky)$.

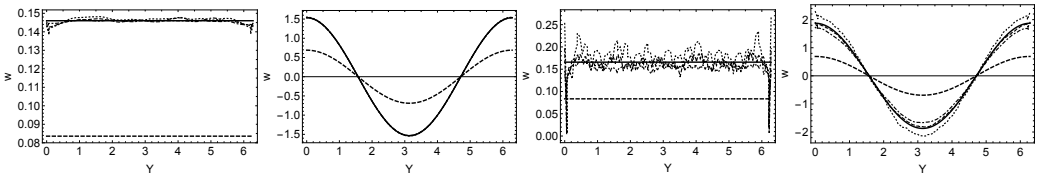

(a) $t = 1/100$,$K = 0$. (b) $t = 1/100$,$K = 1$. (c) $t = 1/1000$,$K = 0$ (d) $t = 1/1000$,$K = 1$.

Figure 15: Parabolic profiles at $x = 0$ (w-component). Triangular penetration pattern. Hole coverage 12%. Three perforated solutions, the reference (dashed), and the effective reference (solid). Loading: $f(x, y) = \cos(Kx)\cos(Ky)$.

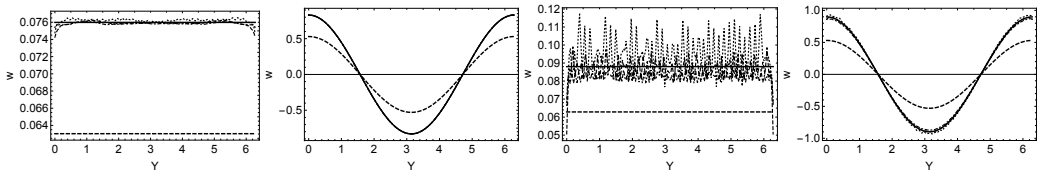

(a) $t = 1/100, K = 0$. (b) $t = 1/100, K = 1$. (c) $t = 1/1000, K = 0$ (d) $t = 1/1000, K = 1$.

Figure 16: Hyperbolic profiles at $x = 0$ (w-component). Regular penetration pattern. Hole coverage 7%. Three perforated solutions, the reference (dashed), and the effective reference (solid). Loading: $f(x, y) = \cos(Kx)\cos(Ky)$.

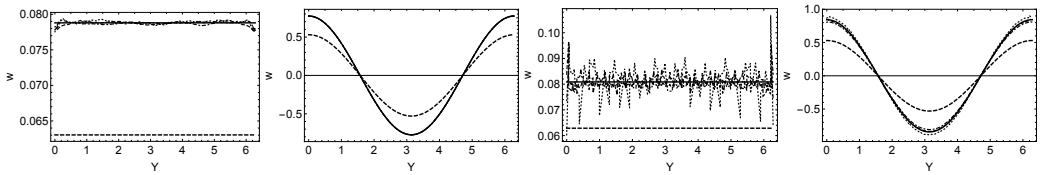

(a) $t = 1/100, K = 0$. (b) $t = 1/100, K = 1$. (c) $t = 1/1000, K = 0$ (d) $t = 1/1000, K = 1$.

Figure 17: Hyperbolic profiles at $x = 0$ (w-component). Triangular penetration pattern. Hole coverage 7%. Three perforated solutions, the reference (dashed), and the effective reference (solid). Loading: $f(x, y) = \cos(Kx)\cos(Ky)$.

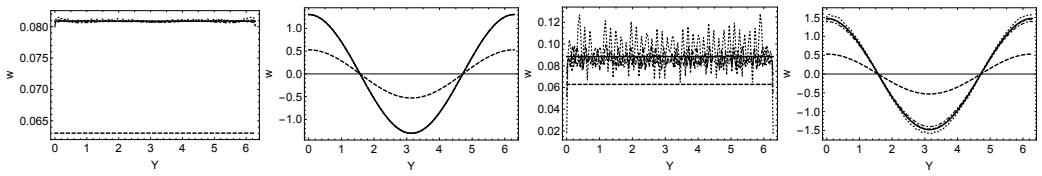

(a) $t = 1/100, K = 0$. (b) $t = 1/100, K = 1$. (c) $t = 1/1000, K = 0$ (d) $t = 1/1000, K = 1$.

Figure 18: Hyperbolic profiles at $x = 0$ (w-component). Regular penetration pattern. Hole coverage 12%. Three perforated solutions, the reference (dashed), and the effective reference (solid). Loading: $f(x, y) = \cos(Kx)\cos(Ky)$.

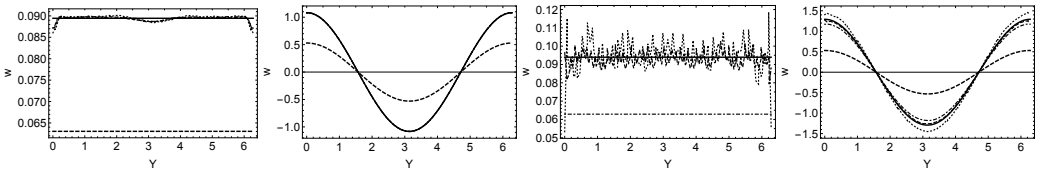

(a) $t = 1/100$,$K = 0$. (b) $t = 1/100$,$K = 1$. (c) $t = 1/1000$,$K = 0$ (d) $t = 1/1000$,$K = 1$.

Figure 19: Hyperbolic profiles at $x = 0$ (w-component). Triangular penetration pattern. Hole coverage 12%. Three perforated solutions, the reference (dashed), and the effective reference (solid). Loading: $f(x, y) = \cos(Kx)\cos(Ky)$.

5.3. Analysis

The results are well aligned with the a priori assumptions on the performance of the different configurations if the boundary layer effect is taken into account. Consistently the values of α decrease as the hole coverage increases and as the dimensionless thickness decreases. The triangular penetration pattern leads to stiffer structures. Interestingly, the hyperbolic shells have larger scaling factors than the parabolic ones. As noted in the introduction, this is an argument against using plate-model derived effective material parameters for shell problems. The effect of the curvature has to be taken into account here. Finally, in the case of constant loading the shells are in membrane dominated state, but if the loading is a Fourier mode with a higher wave number, more bending can occur.

6. Conclusions

Homogenisation of parameter-dependent problems is a difficult problem. In the context of thin shell structures, the central question is to identify the parameter ranges, i.e., dimensionless thicknesses, where the local features do not dominate the solution. Naturally other aspects such as the expected loading or the properties of the penetration patterns play a role as well.

In this paper we outline a strategy for estimating effective material parameters for perforated shells in a reasonably general setting. First, for the given dimensionless thickness one has to find the penetration patterns for which the critical thicknesses are less than the given one. The scaling factor related to the effective material parameter can then be estimated through a minimisation process. The effectiveness of the proposed strategy is demonstrated with a comprehensive set of examples.

Our approach is not limited to source problems but is directly applicable to related important problems such as eigenvalue problems.

References

[1] A. Anand, J. S. Ovall, S. Reynolds, S. Weißer, Trefftz Finite Elements on Curvilinear Polygons, arXiv e-prints (2019) arXiv:1906.09015.

[2] S. Weißer, Arbitrary order trefftz-like basis functions on polygonal meshes and realization in BEM-based FEM, Computers & Mathematics with Applications 67 (2014) 1390 – 1406.

[3] L. Beirão da Veiga, F. Brezzi, A. Cangiani, G. Manzini, L. D. Marini, A. Russo, Basic principles of virtual element methods,, Math. Models Methods Appl. Sci. 23 (2013) 199—214.

[4] H. Martikka, E. Taitokari, Design of perforated shell dryings drums, Mechanical Engineering Research (2012).

[5] M. Forskitt, J. R. Moon, P. A. Brook, Elastic properties of plates perforated by elliptical holes, Applied mathematical modelling (1991).

[6] K. A. Burgemeister, C. H. Hansen, Calculating resonance frequencies of perforated panels, Journal of sound and vibration (1996).

[7] M. J. Jhung, J. C. Jo, Equivalent material properties of perforated plate with triangular or square penetration pattern for dynamic analysis, Nuclear Engineering and Technology (2006).

[8] M. J. Jhung, S. O. Yu, Study on modal characteristics of perforated shell using effective Young's modulus, Nuclear Engineering and Design (2011).

[9] M. J. Jhung, K. H. Jeong, Free vibration analysis of perforated plate with square penetration pattern using equivalent material properties, Nuclear Engineering and Technology (2015).

[10] Korea Institute of Nuclear Safety, Free vibration analysis of perforated cylindrical shell submerged in fluid, Technical Report, KINS/RR-493, 2007.

[11] J. Pitkäranta, A.-M. Matache, C. Schwab, Fourier mode analysis of layers in shallow shell deformations., Computer Methods in Applied Mechanics and Engineering 190 (2001) 2943–2975.

[12] H. Hakula, Y. Leino, J. Pitkäranta, Scale resolution, locking, and high-order finite element modelling of shells, Comput. Methods Appl. Mech. Engrg. 133 (1996) 157–182.

[13] B. Szabo, I. Babuska, Finite Element Analysis, Wiley, 1991.

[14] P. Solin, K. Segeth, I. Dolezel, Higher Order Finite Element Methods, Chapman and Hall/CRC, har/cdr edition, 2003.

[15] P. R. Amestoy, I. S. Duff, J.-Y. L'Excellent, Multifrontal parallel distributed symmetric and unsymmetric solvers, Comput. Methods Appl. Mech. Eng. 184 (2000) 501–520.

[16] P. R. Amestoy, I. S. Duff, J. Koster, J.-Y. L'Excellent, A fully asynchronous multifrontal solver using distributed dynamic scheduling, SIAM Journal on Matrix Analysis and Applications 23 (2001) 15–41.

[17] P. R. Amestoy, A. Guermouche, J.-Y. L'Excellent, S. Pralet, Hybrid scheduling for the parallel solution of linear systems, Parallel Computing 32 (2006) 136–156.